

Article

## Design of an Angle Detector for Laser Beams Based on Grating Coupling

Tapas Kumar Saha <sup>1</sup>, Mingyu Lu <sup>1</sup>, Zhenqiang Ma <sup>2</sup> and Weidong Zhou <sup>1,\*</sup>

<sup>1</sup> Department of Electrical Engineering, University of Texas at Arlington, Arlington, TX 76019, USA; E-Mails: tapaskumar.saha@mavs.uta.edu (T.K.S.); mingyulu@uta.edu (M.L.);

<sup>2</sup> Department of Electrical and Computer Engineering, University of Wisconsin-Madison, Madison, WI 53706, USA; E-Mail: mazq@engr.wisc.edu

\* Author to whom correspondence should be addressed; E-Mail: wzhou@uta.edu; Tel.: +1-817-272-1227; Fax: +1-817-272-7458.

Received: 24 December 2011; in revised form: 21 January 2012 / Accepted: 21 January 2012 /

Published: 1 February 2012

---

**Abstract:** A novel angle detector for laser beams is designed in this paper. It takes advantage of grating coupling to couple the incident light into a slab waveguide; and, the incident light's angle can be determined by reading the outputs of light detectors within the waveguide. This device offers fast-responding on-chip detection of laser beam's angle. Compared to techniques based on quadrant photodiodes or lateral effect photodiodes, the device in this paper has far greater detectable range (up to a few degrees, to be specific). Performance of the laser angle detector in this paper is demonstrated by finite-difference-time-domain simulations. Numerical results show that, the detectable angle range can be adjusted by several design parameters and can reach  $[-4^\circ, 4^\circ]$ . The laser beam angle detector in this paper is expected to find various applications such as ultra-fast optical interconnects.

**Keywords:** diffraction gratings; guided waves; laser beam steering

---

### 1. Introduction

Precise tracking of laser beams has innumerable applications, including but not limited to lidar, chemical/biochemical microsystems, microscopy, optical tweezers, telescopes, satellite communications, and optical interconnects [1,2]. Among these applications, in recent years optical

interconnects have attracted enormous interests particularly [3–5]; and, fast on-chip optical beam detection/tracking/steering techniques are expected to play critical roles in the next-generation optical interconnects [6–8]. The most traditional laser beam detection techniques rely on mechanical steering [9,10]. Although mechanical steering provides broad range of angle detection, it leads to systems that are bulky, complex, costly, and slow. Various contemporary applications (such as optical interconnects) call for low-cost, fast-responding, and on-chip devices for precise beam detection. Quadrant photodiodes (QPDs) may be the most popularly adopted for the purpose of on-chip beam angle detection [11,12]. Other approaches for laser beam angle measurement include lateral-effect photodiodes (LEPs) [13] and dual focus Fresnel lens [14]. Nevertheless, the angle detection methods in [11–14] share one drawback: they can only detect very small angle variations up to 3 mrad or 0.2 degrees.

In this paper, a novel angle detector is designed based on grating coupling. It consists of a grating layer on top of a silicon-on-insulator (SOI) slab waveguide. The incident light is coupled into guided modes within the waveguide via the grating layer, and then, the incident light's angle can be determined by reading the outputs of light detectors within the waveguide. This device offers fast-responding on-chip detection of laser beam's angle, without requiring any external objective lens. Its detectable angle range can reach a few degrees, which is far greater than those associated with QPDs or LEPs. Performance of the laser angle detector in this paper is demonstrated by full-wave finite-difference-time-domain (FDTD) simulations. Numerical results show that, the detectable angle range can be adjusted by several design parameters and can reach  $[-4^\circ, 4^\circ]$ . It is noted that grating coupling was applied to laser angle measurement in the past. For instance, in [15] laser angle was measured based on the spatial variation of the coupled light. Since the measurement precision is dictated by the number of photodetectors placed along the transverse direction of the waveguide, the device in [15] takes large real estate (around 3.5 mm) in order to measure angles up to 1 degree accurately. As a comparison, the detector in this paper only employs two photodetectors and is highly compact: the width of our coupler could be as small as 20  $\mu\text{m}$  (depending on the integration density) with measurement range of  $\pm 4$  degrees.

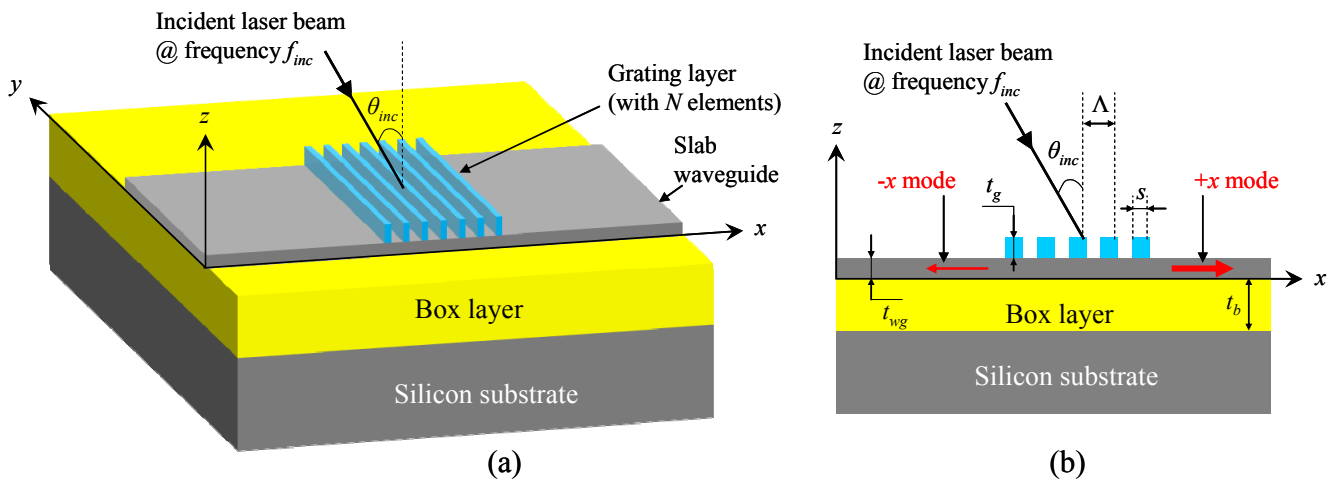
The rest of this paper is organized as follows. The grating-based angle detector is described in Section 2. In Section 3, some numerical results are presented to demonstrate the device's performance. Finally, Section 4 relates to our conclusions of this study.

## 2. Design of the Angle Detector Based on Grating Coupling

Schematic of the grating-based angle detector is depicted in Figure 1. It is completely planar and composed of four layers. The top layer is "grating layer," which consists of  $N$  grating elements. The grating elements are considered uniform and infinitely long along  $y$  direction in our modeling; and, they are deployed periodically along  $x$  direction with periodicity  $\Lambda$ . The grating layer sits on top of an SOI slab waveguide. A laser beam with frequency  $f_{inc}$  is incident onto the device from the top. The incident direction is in the  $x$ - $z$  plane. The angle between the incident laser and  $z$  direction (*i.e.*, surface normal direction) is denoted as  $\theta_{inc}$ . When the laser is incident obliquely,  $\theta_{inc}$  takes positive values when the incident laser is along  $+x$  direction and  $\theta_{inc}$  is negative when the incident laser is along  $-x$  direction. Our device is designed such that the incident light is efficiently coupled to the "+ $x$  traveling

mode” and “ $-x$  traveling mode” in the slab waveguide. When  $\theta_{inc} = 0$  (that is, normal incidence), “ $+x$  mode” and “ $-x$  mode” in the slab waveguide are equally strong, due to the geometrical symmetry. When  $\theta_{inc} \neq 0$  (that is, oblique incidence), the “ $+x$  mode” and “ $-x$  mode” are unbalanced. As a result,  $\theta_{inc}$  can be found by comparing the “ $+x$  mode” and “ $-x$  mode.” In our device, the “ $+x$  mode” and “ $-x$  mode” are observed by placing two detectors in the slab waveguide. The two detectors are named “ $+x$  detector” and “ $-x$  detector,” respectively. The “ $+x$  detector” is placed to the right of the grating structure and it serves to detect the power of the “ $+x$  mode;” similarly, the “ $-x$  detector” is placed to the left of the grating structure and it detects the power of the “ $-x$  mode.” The photodetectors in the waveguide can be implemented by following available architectures in [16–18].

**Figure 1.** (a) The device schematic. (b) The cross-section view in the  $x$ – $z$  plane.



In Figure 2, typical spectral outputs of the “ $+x$  detector” are illustrated with various  $\theta_{inc}$  values. In our design, the incident light is coupled to the waveguide modes via the second-order Floquet mode predominantly. Consequently, transverse resonance occurs when the following condition is satisfied

$$k_{inc} \sin \theta_{inc} + 2 \frac{2\pi}{\Lambda} = k_x^{wg} \tag{1}$$

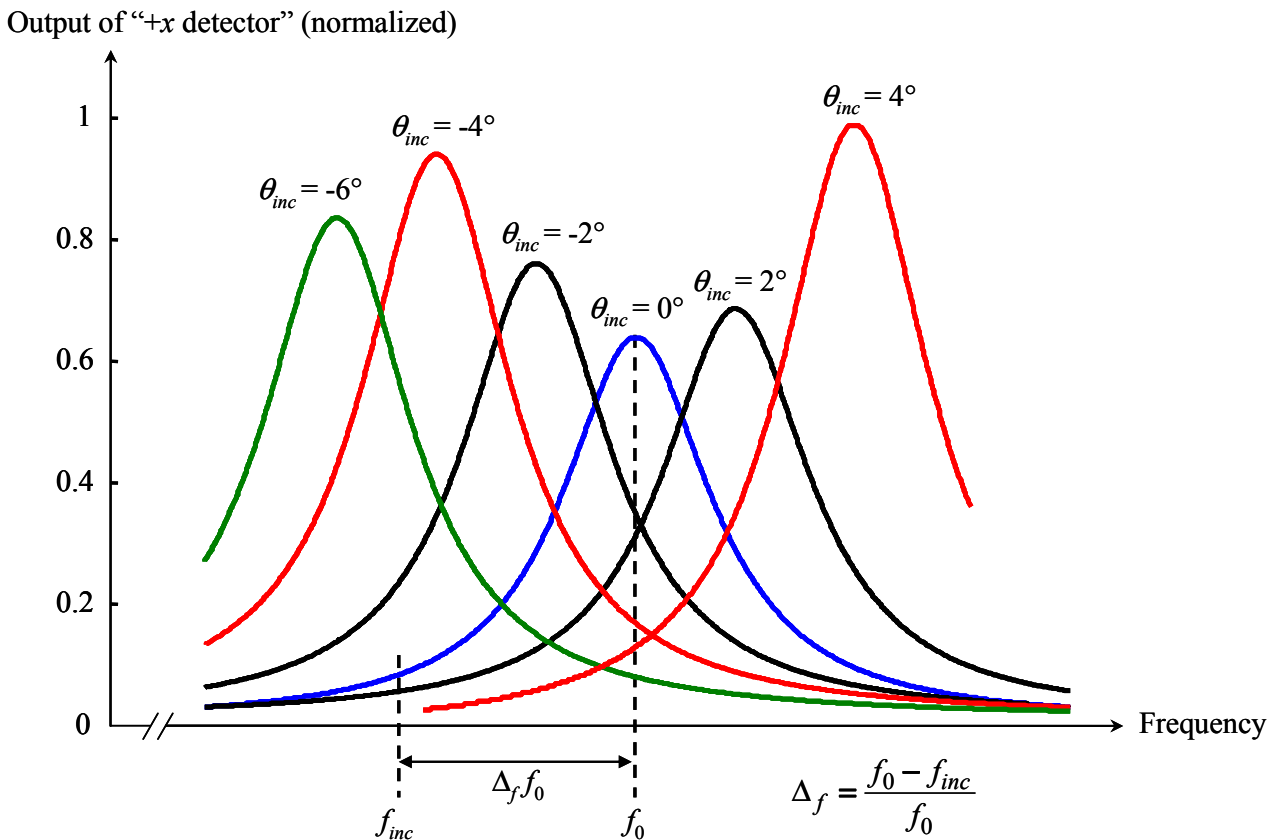
In the above equation,  $k_{inc} = 2\pi f_{inc}/c$ ,  $c$  is the speed of light in free space, and  $k_x^{wg}$  is the wavenumber along  $x$  for the fundamental guided mode in the slab waveguide. It is noted that  $k_x^{wg}$  is non-linear with respect to the frequency. The transverse resonant frequency for  $\theta_{inc} = 0$  is denoted as “ $f_0$ .” The transverse resonant frequency increases with the increase of  $\theta_{inc}$ , as shown in Figure 2. Bandwidth of the resonance is measured by finding the frequencies at which the photodetector’s output drops by 3 dB with respect to the value at the resonant frequency. Further, quality factor is defined as the ratio between the resonant frequency and the bandwidth.

In our design,  $f_0$  is chosen to be close to  $f_{inc}$  and greater than  $f_{inc}$ ; and, the offset between  $f_0$  and  $f_{inc}$  is characterized by

$$\Delta_f = \frac{f_0 - f_{inc}}{f_0} \tag{2}$$

Output of the “+x detector” varies with respect to  $\theta_{inc}$  when  $f_{inc}$  is a constant frequency. Meanwhile, output of the “-x detector” exhibits variation with respect to  $\theta_{inc}$  as well. It is not a difficult task to sketch the outputs of the “-x detector” based on Figure 2, as negative  $\theta_{inc}$  for the “-x detector” is equivalent to positive  $\theta_{inc}$  for the “+x detector.” Since  $f_0$  and  $f_{inc}$  are close to each other, it is possible to derive the value of  $\theta_{inc}$  by observing the outputs of the two detectors if the incident direction is not far off the normal direction. If  $\theta_{inc}$  is too large, the outputs of both “+x detector” and “-x detector” would be too weak and hence unreliable. In order to enlarge the detectable range of  $\theta_{inc}$ , one feasible way is to reduce the device’s quality factors because lower quality factors lead to wider bandwidths for the curves in Figure 2. Nevertheless, wider bandwidths unavoidably diminishes the detection sensitivity for  $\theta_{inc}$ . Other than quality factors, another important design parameter is  $\Delta_f$ . It is observed that, larger  $\Delta_f$  results in larger detectable range for  $\theta_{inc}$ . However, large  $\Delta_f$  reduces the coupling efficiencies around  $\theta_{inc}=0$ . In Section 3, the device’s performances with respect to various design parameters are shown by some numerical results.

Figure 2. Illustration of the angle detector’s rationale.



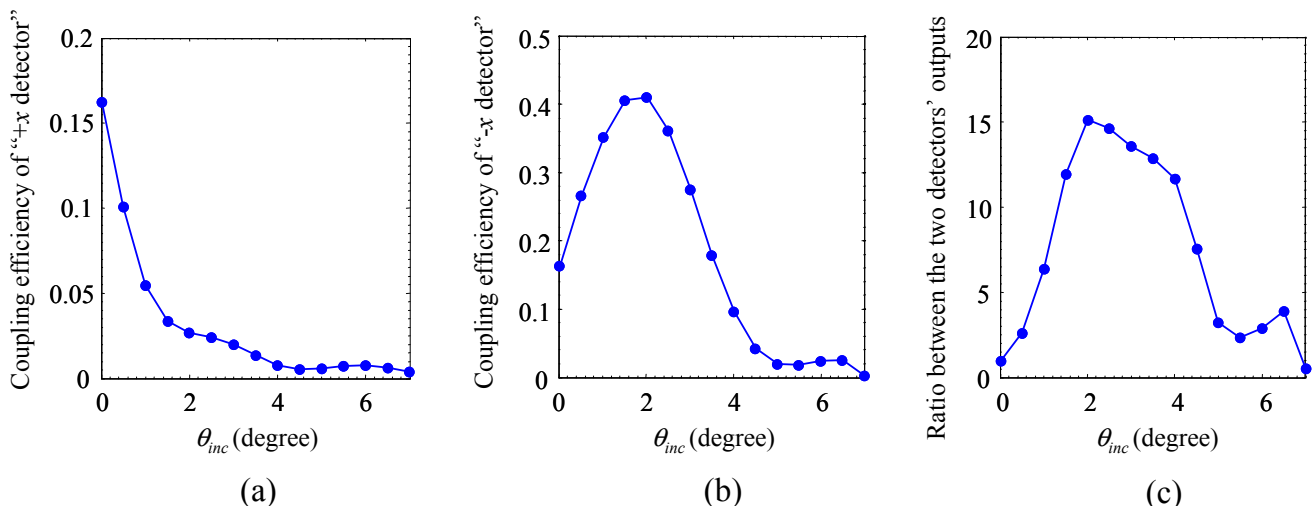
### 3. Numerical Results

In this section, some numerical results are presented to demonstrate the performance of the angle detector described in the previous section. Specifically, the angle detector shown in Figure 1 is simulated by MEEP [19], which is a full-wave solver based on FDTD method. MEEP has been widely used to characterize various photonic devices, and its fidelity has been verified extensively [20–22].

All the numerical results in this section are obtained with the following geometrical parameters:  $\Lambda = 1.065 \mu\text{m}$ ,  $s = 0.234 \mu\text{m}$ ,  $t_g = 0.26 \mu\text{m}$ ,  $t_{wg} = 0.22 \mu\text{m}$ , and  $t_b = 2 \mu\text{m}$ , (please refer to Figure 1 for the definitions of these parameters; thickness of the substrate has negligible impact on the device, according to our observations). The refraction index of box layer is 1.48; and, the other three layers are made of silicon with refraction index 3.48. The incident light is a Gaussian beam with waist radius  $23.4 \Lambda$  and frequency  $f_{inc} = 0.646 c/a$ , where  $a = 1 \mu\text{m}$ ; in addition, electric field of the incident light is polarized along  $y$  direction. The two detectors are modeled by integrating the Poynting vectors along  $+x$  or  $-x$  direction within the waveguide. As for each detector, coupling efficiency is defined as  $P_d/P_{inc}$ , where  $P_d$  is the detector's output and  $P_{inc}$  is calculated by integrating the incident light's power density by the detector's aperture. As discussed in Section 2, our device's performance is dictated by two major design parameters: quality factors and  $\Delta_f$ . In the remainder of this section, various values of these two design parameters are employed to adjust the angle detector's performance. The quality factors are controlled by  $N$ , the number of grating elements (apparently, the larger  $N$  is, the higher the quality factors are).

Outputs of the “ $+x$  detector” and “ $-x$  detector” are plotted in Figure 3(a,b) respectively, with  $\Delta_f = 0.88\%$  and  $N = 31$ . Since  $f_{inc} < f_0$  in our design, the “ $-x$  output” is stronger than the “ $+x$  output” for positive  $\theta_{inc}$ . The choice of  $\Delta_f$  makes  $f_{inc}$  coincide with the transverse resonant frequency of  $\theta_{inc} = 2^\circ$  for the “ $-x$  detector.” As a result, when the ratio between “ $-x$  output” and “ $+x$  output” is plotted in Figure 3(c), it exhibits a steep increasing slope in range  $\theta_{inc} \in [0, 2^\circ]$ . When  $\theta_{inc}$  is negative, the two detectors' outputs would be “exchanged:” the ratio between “ $+x$  output” and “ $-x$  output” exhibits a steep slope in range  $\theta_{inc} \in [-2^\circ, 0]$ . The data for negative  $\theta_{inc}$  are symmetric to those for positive  $\theta_{inc}$ , hence are not shown in Figure 3. Therefore, from the two detectors' outputs,  $\theta_{inc}$  can be reliably derived when it falls in the range  $-2^\circ < \theta_{inc} < 2^\circ$ .

**Figure 3.** Numerical results for the angle detector. (a) Coupling efficiency of the “ $+x$  detector.” (b) Coupling efficiency of the “ $-x$  detector.” (c) Ratio between the two detectors' outputs.

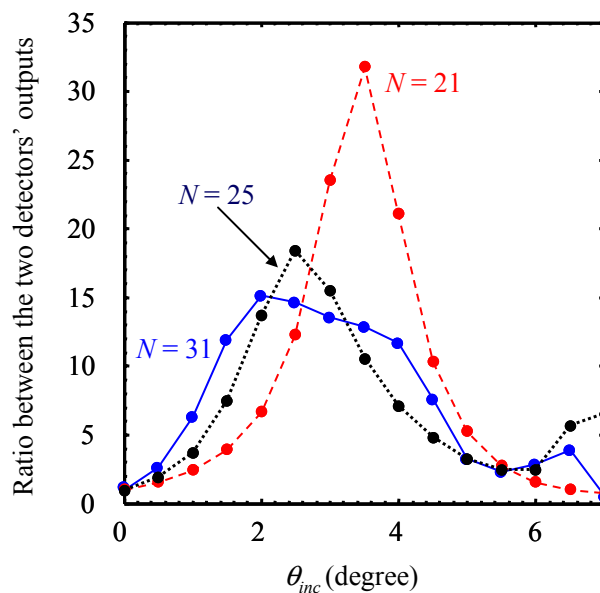


As analyzed in Section 2, the detectable range for  $\theta_{inc}$  can be enlarged by reducing the quality factors. This analysis is verified by numerical results in Figure 4. There are three curves in Figure 4. One of them is the same as that in Figure 3(c), with  $N = 31$ . On the basis of the curve in Figure 3(c),

the other two curves in Figure 4 are obtained with  $N = 25$  and  $N = 21$ . As expected, the reduction of  $N$  diminishes the device’s quality factors, and thus, increases the detectable range. To be specific, the detectable range is  $[-2^\circ, 2^\circ]$  when  $N = 31$ ; it is increased to  $[-2.5^\circ, 2.5^\circ]$  with  $N = 25$  and further increased to  $[-3.5^\circ, 3.5^\circ]$  with  $N = 21$ . Nevertheless, the curves of “ $N = 21$ ” and “ $N = 25$ ” have smaller slopes in the range  $[0, 2^\circ]$  compared to the slope of “ $N = 31$ ” curve, which means that lower quality factors result in lower measurement sensitivity for  $\theta_{inc}$ .

Figure 5 serves to demonstrate the impact of  $\Delta_f$  on the device’s performance. One of the two curves in Figure 5 is the same as that in Figure 3(c), where  $\Delta_f = 0.88\%$ . The other curve in Figure 5 is generated by increasing  $\Delta_f$  to 1.03% and with all the other parameters unchanged. It is observed that, the increase of  $\Delta_f$  enlarges the detectable range from  $[-2^\circ, 2^\circ]$  to  $[-4^\circ, 4^\circ]$ . As a price, the coupling efficiencies around  $\theta_{inc} = 0$  drop with the increase of  $\Delta_f$ . To be specific, the coupling efficiencies of both detectors at surface normal incidence are 17% when  $\Delta_f = 0.88\%$ ; and they drop to 11% when  $\Delta_f$  increases to 1.03%.

**Figure 4.** Numerical results for the angle detector with three different values of  $N$ .



In order to visualize our device’s behavior better, field distributions are plotted in Figure 6 for several incident angles. The field distribution plots in Figure 6 correspond to the  $\Delta_f = 1.03\%$  curve of Figure 5. The device configuration is shown in Figure 6(a). The incident wave is a continuous wave at  $f_{inc} = 0.645 c/a$ . In Figure 6(b–e), electric field  $E_y$  at a certain time moment is plotted, with four different incident angles respectively. In Figure 6(b–e), the strongest positive field intensity is represented by dark red color, the strongest negative field intensity is represented by dark blue color, and white color stands for zero field intensity, as specified at the end of Figure 6. Two guided modes (which are traveling toward  $+x$  and  $-x$  directions, respectively) can be clearly identified in the waveguide. When  $\theta_{inc} = 0$ , the two modes are equally strong. With the increase of incident angle, the two modes become more and more unbalanced. When  $\theta_{inc} = 3^\circ$ , the  $-x$  mode is much stronger than the  $+x$  mode.

**Figure 5.** Numerical results for the angle detector with two different values of  $\Delta_f$ .

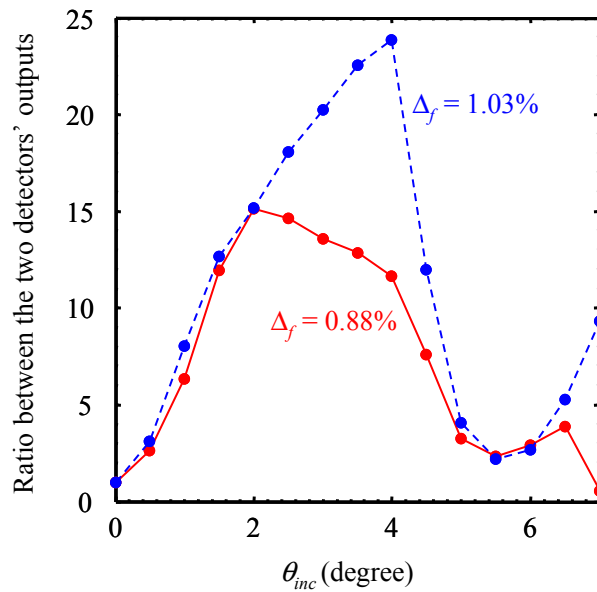
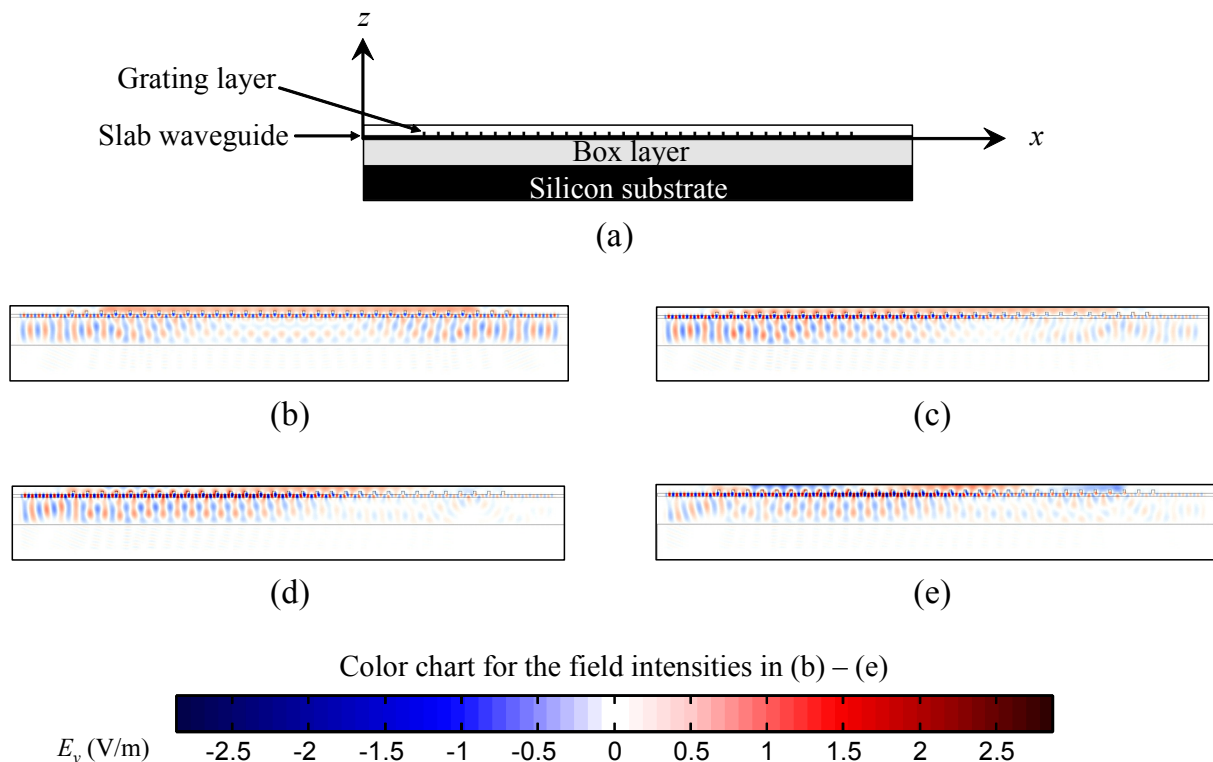


**Figure 6.** Field distribution plots with four different incident angles. (a) Device configuration. (b) Field distribution plot with  $\theta_{inc} = 0^\circ$ . (c) Field distribution plot with  $\theta_{inc} = 1^\circ$ . (d) Field distribution plot with  $\theta_{inc} = 2^\circ$ . (e) Field distribution plot with  $\theta_{inc} = 3^\circ$ .



#### 4. Conclusions

In this paper, a novel device is designed to detect the angle of a laser beam. It consists of a grating layer on top of an SOI slab waveguide. The incident light is coupled into guided modes within the waveguide via the grating layer, and the incident light's angle can be determined by reading the

outputs of light detectors within the waveguide. This device offers fast-responding on-chip detection of laser beam's angle, with detectable angle range far greater than conventional techniques like QPDs and LEPs. Performance of the laser angle detector in this paper is demonstrated by full-wave FDTD simulations. Numerical results show that the detectable angle range can be adjusted by several design parameters and can reach  $[-4^\circ, 4^\circ]$ . Efforts on experimental verification of the grating-based angle detector are currently ongoing. According to our observations, it is challenging to achieve high measurement accuracy with large detectable angle range. We are currently investigating an innovative calibration scheme to improve the accuracy of angle measurement for our device.

### Acknowledgments

This work is supported in part by US AFOSR MURI program under Grant FA9550-08-1-0337, by AFRL CONTACT program under Grant FA8650-07-2-5061, and in part by US ARO under Grant W911NF-09-1-0505.

### References and Notes

1. Mawatari, K.; Shimoide, K. Reflective thermal lens detection device. *Lab Chip* **2006**, *6*, 127-130.
2. Müller, H.; Chiow, S.-W.; Long, Q.; Vo, C.; Chu, S. Active sub-Rayleigh alignment of parallel or antiparallel laser beams. *Opt. Lett.* **2005**, *30*, 3323-3325.
3. Mukai, S.; Watanabe, M.; Itoh, H.; Yajima, H.; Hosoi, Y.; Uekusa, S. Beam scanning and switching characteristics of twin-striped lasers with a reduced stripe spacing. *Opt. Quant. Electron.* **1985**, *17*, 431-434.
4. Scifres, D.R.; Streifer, W.; Burnham, R.D. Beam scanning with twin-stripe injection-lasers. *Appl. Phys. Lett.* **1978**, *33*, 702-704.
5. Kurosaka, Y.; Iwahashi, S.; Liang, Y.; Sakai, K.; Miyai, E.; Kunishi, W.; Ohnishi, D.; Noda, S. On-chip beam-steering photonic-crystal lasers. *Nat. Photon.* **2010**, *4*, 447-450.
6. Tuantranont, A.; Bright, V.M.; Zhang, J.; Zhang, W.; Neff, J.A.; Lee, Y.C. Optical beam steering using MEMS-controllable microlens array. *Sensors Actuat. A: Phys.* **2001**, *91*, 363-372.
7. May-Arrijoja, D.A.; Bickel, N.; LiKamWa, P. Optical beam steering using InGaAsP multiple quantum wells. *IEEE Photonic Technol. Lett.* **2005**, *17*, 333-335.
8. Jarrahi, M.; Fabian, R.; Pease, W.; Miller, D.A.B.; Lee, T.H. High-speed optical beam-steering based on phase-arrayed waveguides. *J. Vac. Sci. Technol. B* **2008**, *26*, 2124-2126.
9. Nakamura, O.; Goto, M.; Toyoda, K.; Takai, N.; Kurosawa, T.; Nakamata, T. A laser tracking robot-performance calibration system using ball-seated bearing mechanisms and a spherically shaped cat's-eye retroreflector. *Rev. Sci. Instr.* **1994**, *65*, 1006.
10. Umetsu, K.; Furutnani, R.; Osawa, S.; Takatsuji, T.; Kurosawa, T. Geometric calibration of a coordinate measuring machine using a laser tracking system. *Meas. Sci. Technol.* **2005**, *16*, 2466-2472.
11. Manojlovic, L.M.; Barbaric, Z.P. Optimization of optical receiver parameters for pulsed laser-tracking systems. *IEEE Trans. Instrum. Meas.* **2009**, *58*, 681-690.
12. Toyoda, M.; Araki, K.; Suzuki, Y. Measurement of the characteristics of a quadrant avalanche photodiode and its application to a laser tracking system. *Opt. Eng.* **2002**, *41*, 145-149.

13. Makynen, A.; Kostamovaara, J.T.; Myllyla, R.A. Displacement sensing resolution of position-sensitive detectors in atmospheric turbulence using retroreflected beam. *IEEE Trans. Instrum. Meas.* **1997**, *46*, 1133-1136.
14. Fujita, T.; Nakamura, K.; Matozaki, T. Simple and accurate propagation-angle observation of a collimated laser beam within a short optical path range by use of a dual-focus Fresnel lens. *Opt. Rev.* **2005**, *12*, 260-263.
15. Kunz, R.E.; Dubendorfer, J. Novel miniature integrated optical goniometers. *Sensor Actuat. A: Phys.* **1997**, *60*, 23-28.
16. Roelkens, G.; Van Thourhout, D.; Baets, R.; Notzel, R.; Smit, M. Laser emission and photodetection in an InP/InGaAsP layer integrated on and coupled to a Silicon-on-Insulator waveguide circuit. *Opt. Express* **2006**, *14*, 8154-8159.
17. Liang, D.; Fiorentino, M.; Okumura, T.; Chang, H.-H.; Spencer, D.T.; Kuo, Y.-H.; Fang, A.W.; Dai, D.; Beausoleil, R. G.; Bowers, J. E., Electrically-pumped compact hybrid silicon microring lasers for optical interconnects. *Opt. Express* **2009**, *17*, 20355-20364.
18. Roelkens, G.; Brouckaert, J.; Taillaert, D.; Dumon, P.; Bogaerts, W.; Van Thourhout, D.; Baets, R.; Notzel, R.; Smit, M. Integration of InP/InGaAsP photodetectors onto silicon-on-insulator waveguide circuits. *Opt. Express* **2005**, *13*, 10102-10108.
19. Meep. Available online <http://ab-initio.mit.edu/wiki/index.php/Meep> (accessed on 30 January 2012).
20. Yang, X.; Yu, M.; Kwong, D.-L.; Wong, C.W. Coupled resonances in multiple silicon photonic crystal cavities in all-optical solid-state analogy to electromagnetically induced transparency. *IEEE J. Sel. Top. Quantum Electr.* **2010**, *16*, 288-294.
21. Baumann, K.; Stoferle, T.; Moll, N.; Raino, G.; Mahrt, R.F.; Wahlbrink, T.; Bolten, J.; Scherf, U. Design and optical characterization of photonic crystal lasers with organic gain material *J. Opt.* **2010**, *12*, 065003.
22. Kim, T.-T.; Lee, S.-G.; Kim, S.-H.; Kim, J.-E.; Park, H. Y.; Kee, C.-S., Ring-type Fabry-Perot filter based on the self-collimation effect in a 2D photonic crystal. *Opt. Express* **2010**, *18*, 17106-17113.